Temporal variation of the spatial density distribution above a nanosecond pulsed dielectric barrier discharge plasma actuator in quiescent air

Takahiro Ukai, Andrew Russell, Hossein Zare-Behtash, and Konstantinos Kontis

---

Articles you may be interested in

Numerical investigation of nanosecond pulsed plasma actuators for control of shock-wave/boundary-layer separation
Physics of Fluids **30**, 106105 (2018); 10.1063/1.5051823

Unsteady shock interactions on V-shaped blunt leading edges
Physics of Fluids **30**, 116104 (2018); 10.1063/1.5051012

Effect of boundary layer thickness on transverse sonic jet mixing in a supersonic turbulent crossflow
Physics of Fluids **30**, 115104 (2018); 10.1063/1.5056540

Numerical investigation of coalescence-induced self-propelled behavior of droplets on non-wetting surfaces
Physics of Fluids **30**, 112102 (2018); 10.1063/1.5046056

Numerical investigation of internal solitary waves of elevation type propagating on a uniform slope
Physics of Fluids **30**, 116602 (2018); 10.1063/1.5050568

Effects of pulse polarity on nanosecond pulse driven dielectric barrier discharge plasma actuators
Journal of Applied Physics **115**, 043306 (2014); 10.1063/1.4863175

Temporal variation of the spatial density distribution above a nanosecond pulsed dielectric barrier discharge plasma actuator in quiescent air

Takahiro Ukai,[1,a] Andrew Russell,[2] Hossein Zare-Behtash,[2] and Konstantinos Kontis[2]

[1]*Osaka Institute of Technology, Osaka 535-8585, Japan*
[2]*School of Engineering, University of Glasgow, Glasgow G12 8QQ, United Kingdom*

The thermal perturbation caused by a nanosecond pulsed dielectric barrier discharge (ns-DBD) plasma actuator may lead to boundary layer transition. Hence, understanding of the thermal flow induced by the ns-DBD plasma actuator will contribute to the development of an efficient flow control device for various engineering applications. In this study, the spatial density distribution related to the thermal flow was experimentally investigated using both qualitative and quantitative schlieren techniques. The focus of this study is to understand the initial temporal variation of the spatial density distribution above the ns-DBD plasma actuator in quiescent air. The quantitative visualisation showed that a hot plume is generated from the edge of the exposed electrode and moves slightly towards the ground electrode. A possible explanation is that an ionic wind and/or an induced jet leads to the movement of the hot plume. However, the plasma-induced flow (the ionic wind and the induced jet) is generated after the primary plasma discharges; namely, the hot plume does not move immediately after the first plasma discharge. At almost the same time as the movement of the hot plume, consecutive plasma discharges enhance the density of the hot plume; thereafter, the density reaches almost a steady state. *Published by AIP Publishing.* https://doi.org/10.1063/1.5054263

I. INTRODUCTION

Dielectric barrier discharge (DBD) plasma actuators are promising devices for flow control that can be applied to a number of scenarios: flow separation postponement, turbulence augmentation, drag reduction, and lift enhancement. Many numerical and experimental investigations have shown the effectiveness of DBD plasma actuators for engineering applications, such as film cooling,[1,2] aircraft wing,[3–5] and ground vehicles.[6,7] The experiment of Benard *et al.*[8] demonstrated that the DBD plasma actuator placed on an NACA0015 aircraft wing delays the onset of a stall by one or two degrees and achieved approximately 30% drag reduction at a 15° incidence. According to Choi *et al.*,[9] multiple DBD plasma actuators would contribute to skin-friction reduction due to the induced quasi-streamwise vortices in the turbulent boundary layer. Moreover, Roy *et al.*[6] showed that a serpentine DBD plasma actuator, positioned at the rear body of a lorry, induces the streamwise vortices and demonstrated that a 10% drag reduction is achieved at a freestream velocity of 31.3 m/s. However, what is important to note is that the aerodynamic performance depends on the actuator configuration and the installation position,[10–12] as well as electrical parameters, magnitude of input voltage, frequency, duty cycle, etc.[8,11–14] The input voltage waveform has been shown to have a particularly dramatic effect on induced-flow characteristics.

Nanosecond pulsed DBD (ns-DBD) plasma actuators are potentially applicable to the high-speed flow regime. The previous studies demonstrated that a nanosecond plasma actuator influences the flow field at a Mach 0.85[3] and a Mach 2.8.[15] The ac-driven DBD (ac-DBD) plasma actuator, which is excited by a sinusoidal input voltage signal, produces an ionic wind that induces a body force close to the surface of the dielectric. However, the induced-flow velocity of the ac-DBD plasma actuator is in the range of only a few meters per second (usually less than 10 m/s) in quiescent air;[11] therefore, its application to high-speed flows is limited. On the other hand, the ns-DBD plasma actuator, which is excited by short pulsed high voltage, in the order of nanoseconds, is applicable to the aerofoil flow reattachment up to Mach 0.85.[3] Instead of the body force, the ns-DBD plasma actuator provides energy transfer which is a dominant induced-flow characteristic.[16] The rapid temperature increase is caused by the high voltage energy deposition from the nanosecond pulsed discharge, which results in shock wave formation due to the instantaneous heating of the gas. A hemi-cylindrical shock wave is generated along the edge of the exposed electrode. Moreover, a plasma layer which propagates towards the dielectric surface generates weak shock waves which coalesce into a quasi-planar shock wave.[17] Therefore, the ns-DBD plasma actuator acts as a thermal energy source resulting in the rapid localised heating of the near-surface gas layer at the plasma actuator. This outlines the difference in induced-flow characteristics between the ac-DBD and ns-DBD plasma actuators.

The energy transfer generated by ns-DBD plasma actuators results in dominant flow control authority. Induced flow characteristics in a quiescent gas condition were numerically and experimentally investigated in the previous studies.[18–20] Zhao *et al.*[20] investigated a shock Mach number in various input voltages and showed that the shock Mach number which depends on the input voltages decays quickly and it propagates

---
a)Author to whom correspondence should be addressed: takahiro.ukai@oit.ac.jp. Telephone: +81-(0)6-6954-4256.

30, 116106-1

at approximately Mach 1 from 2 or 3 mm from the plasma surface. Additionally, ns-DBD plasma actuators lead to thermal perturbation with the weak shock wave. According to an experimental investigation in a quiescent gas condition,[18] the area of the hot spot expands with the increase of the number of input voltage pulses within the burst. From the point of view of flow modification, the weak shock wave should not strongly influence surrounding air at the high-speed flow. However, the ns-DBD plasma actuator is applicable up to Mach 0.85.[3] The reason why the ns-DBD plasma actuators can change the surrounding flow is that the thermal perturbation plays a key role rather than the shock wave.

To understand thermal flow induced under the uniform flow condition, the previous studies attempted to investigate the effects of the thermal perturbation on surrounding air.[18,21–24] Komuro *et al.*[21] investigated the effect of the thermal perturbation on flow instability due to a ns-DBD plasma actuator around the aerofoil at 20 m/s and showed that the interaction of two different heated structures improved the lift performance of the aerofoil. Correale *et al.*[18] investigated the influence of the heated gas on a laminar boundary layer on a flat plate. They showed that the thermal perturbation generated by the plasma discharge leads to a velocity fluctuation, and it is believed that the velocity fluctuation results in a T-S (Tollmien-Schlichting) wave which causes laminar-turbulent transition of the boundary layer. Therefore, the thermal perturbation plays a key role in the flow control mechanism of the ns-DBD. The thermal perturbation is associated with the actuation frequency of the ns-DBD plasma actuator, and the actuation frequency influences the boundary layer instability. According to an experimental investigation regarding boundary layer transition by the ns-DBD plasma actuator,[23] the boundary layer transition point moves upstream when the actuation frequency increases. Moreover, the thermal perturbation would create coherent vortices that increase the momentum transfer from the freestream flow to the boundary layer. Such vortices generated by ns-DBDs also result in the reattachment of the separated flow on an aircraft wing.[24] Additionally, a hot wire experiment by Ullmer *et al.*[23] revealed that a ns-DBD plasma actuator excited velocity oscillations inside a boundary layer. This means that the ns-DBD plasma actuators generate turbulent kinetic energy in the boundary layer. Although the hot wire and liquid crystal techniques provide the valuable quantitative information, the quantitative spatial measurement techniques lead to further understanding of the mechanism of the boundary layer transition.

The performance of the ns-DBD plasma actuator is significant in the high-speed flow regime, and the instant heating influences boundary layer transition. However, the mechanism by which the instant heating affects the flow instability is not fully understood. The investigations about the thermal distribution generated by the ns-DBD plasma actuator in the quiescent gas condition are important to elucidate how the surrounding gas is heated, and there is a local heat spot. It is believed that the investigations of the thermal distribution in a quiescent gas condition lead to deeper understanding of the mechanism of the boundary layer transition. Additionally, the previous investigations found that thermal flow is important for flow control rather than the shock wave; however, the

quantitative investigation of the temporal and spatial variations of a density/temperature is necessary to further understanding the mechanism of thermal flow by the ns-DBD plasma actuator. In this study, to understand the thermal perturbation induced by the ns-DBD plasma actuator, the spatial density field in quiescent air was experimentally investigated using the qualitative and quantitative schlieren techniques.

II. EXPERIMENTAL SETUP AND DIAGNOSTICS

A. Experimental model

An ns-DBD plasma actuator shown in Fig. 1 was used in the present study. In a previous study,[25] the effect of geometry on shock wave strength was investigated, and the results showed that the thicker dielectric provides a stronger shock wave for a given input voltage and pulse frequency. The optimal geometric parameters employed in the previous study (electrode thickness and electrode width) were selected for the present investigation. The exposed high-voltage electrode of 5 mm in width and the ground electrode of 10 mm in width were made of copper with a thickness of 35 μm. The electrodes are separated by a dielectric material (FR-4: Flame Retardant Type 4) with a thickness of 0.4 mm. The material of the plasma actuator is manufactured by the company MG Chemicals. There is no discharge gap between the electrodes. The lateral length of all electrodes is 90 mm. The ground electrode was fully covered by three layers of the polyimide film, and the thickness of each polyimide film is approximately 70 μm. The polyimide film covered the exposed electrode 9 mm from both lateral side edges to avoid a plasma discharge from the side edges, plasma releases from the exposed electrode of 72 mm in width. The actuators were made using the process of double-sided photolithography. The masks for the process were created using CAD software (SolidWorks) to ensure their accuracy as much as possible. The copper comes with a photo resist coating; this is exposed under UV light for 30 s. It is then put in a developer bath that removes the resist that was exposed to the UV light. The developer is Seno 4006, a solution of potassium hydroxide and disodium metasilicate. The board is then sprayed with a ferric chloride solution to remove the exposed copper. It takes approximately 1 min per side to remove the copper. Once the copper is removed, the remaining photo resist is cleaned with acetone.

The discharge is driven by a high-voltage nanosecond pulse generator [Megaimpulse, model: NPG-18/3500(N)] that supplies negative pulse polarity at a pulse rise time of approximately 4 ns. In the present study, an input voltage of 12 kV
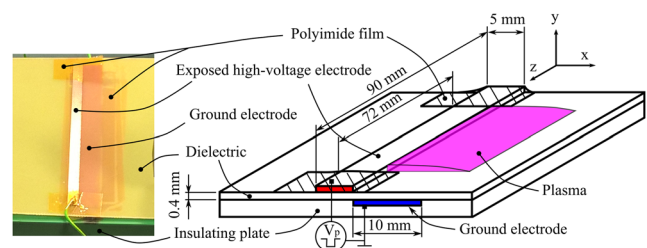

FIG. 1. The configuration of the ns-DBD plasma actuator (left figure: the actual plasma actuator used in the study).

(negative polarity) was used with a pulse frequency of 1 kHz controlled by a function generator (AIM & THURLBY THANDAR INSTRUMENTS, model: TG2000). As the negative polarity produces large gross energy related to strong gas heating,[26] thus negative polarity was used in this study. The supplied high-voltage pulses were transferred from the pulse generator to the exposed electrode by a 75 Ω coaxial cable.

The ambient temperature was monitored using a K-type thermocouple with a data acquisition module system (National Instruments Corp., model: NI-9213, 24 bit) driven by Lab-VIEW. The ambient pressure was measured by a Fortin mercury barometer. In the present experiment, the ambient temperature and ambient pressure were 288.7 ± 0.3 K and 101.38 ± 0.03 kPa, respectively.

B. Conventional schlieren photography

The schlieren technique with a standard Z-type optical arrangement was employed to visualise the qualitative density gradient above the ns-DBD plasma actuator that leads to the generation of a shock wave as well as a thermal distribution. The schlieren system consists of a continuous light source (Newport, model: 66921) with a 450 W Xe arc lamp, a condenser lens with a focal length of 70 mm, a pinhole, a pair of 203.3 mm diameter concave mirrors with a focal length of 1829 mm, a circular dot cut-off plate, an imaging lens, and a high-speed camera. The pinhole in front of the condenser lens creates a light spot that illuminates the first concave mirror. The light beam is then collimated by the first mirror and passes through the test section where the ns-DBD plasma actuator is located. The collimated beam is reflected by the second concave mirror. The circular dot plate is positioned at the focal point of the second mirror. The circular dot plate plays the same role as a knife edge, but the density change in both directions on the x-y plane is made visible simultaneously. The imaging lens in front of the camera focuses the image onto the camera sensor. The images were acquired using a 10 bit CMOS camera (Photron, model: FASTCAM-APX RS, maximum spatial resolution: 1024 × 1024 pixels) at a frame rate of 70 kfps with an exposure time of 1 μs. An offset angle between the collimated light beam and the light path from the light source to the first/second mirrors was set at 19° to prevent coma aberration. To transfer from pixels to millimetres, we took the image of an object where the actual size was known. In colour schlieren mode, a three colour filter wheel was used as a substitute for the circular dot plate. The colour images were recorded using a high resolution CMOS colour camera (Canon, model: EOS 600D, 18 Mpixels resolution). The camera is set to continuous shooting mode at 3.7 fps, while the shutter speed is set at a minimum of 0.25 ms. As the nanosecond pulsed generators generate electromagnetic interference (EMI), the data acquisition system and camera were covered using a metal mesh to minimize the effect of the EMI as much as possible.

C. Calibrated schlieren photography

The calibrated schlieren technique enables the measurement of the quantitative spatial density field above the ns-DBD plasma actuator. The optical arrangement of calibrated schlieren photography is shown in Fig. 2 which is the same as
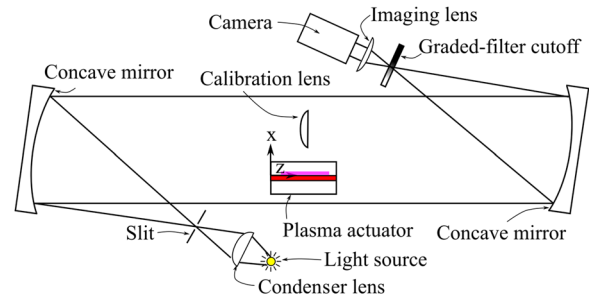

FIG. 2. Optical arrangement of the calibrated schlieren photography.

that of the conventional high-speed schlieren photography previously discussed. However, several optical items are the difference between these setups. A graded filter, which plays the same role as a knife edge, was substituted for the circular dot plate, and the pinhole was replaced with a slit. The graded filter spreads the cutoff linearly in the beam focal plane and lessens the diffraction effect of the knife edge.[27] The graded filter and the slit were vertically positioned to measure a pixel intensity change in the x-direction, whereas they were horizontally positioned for a pixel intensity change in the y-direction. Both pixel intensity changes in the x- and y-components are necessary because the density gradient in the x- and y-components is apparent above the plasma actuator. The images were acquired using the same Photron camera (FASTCAM-APX RS) at a frame rate of 3 kfps with an exposure time of 22.11 μs. This experiment focuses on the quantitative visualisation of the thermal distribution rather than shock wave propagation; therefore, the exposure time is relatively longer than that used for shock wave visualisation.

The principle of the quantitative schlieren technique is explained here. The angle of the refraction ε obtained from refractive-index gradient integrated along the optical axis (the z-direction shown in Fig. 1) above the plasma actuator is expressed as

$$\varepsilon_y = \frac{1}{n} \int_0^Z \frac{\partial n(x,y)}{\partial y} dZ = \frac{Z}{n_\infty} \frac{\partial n(x,y)}{\partial y}, \tag{1}$$

$$\varepsilon_x = \frac{1}{n} \int_0^Z \frac{\partial n(x,y)}{\partial x} dZ = \frac{Z}{n_\infty} \frac{\partial n(x,y)}{\partial x}. \tag{2}$$

The subscript ∞ denotes the quiescent surrounding gas, and n is the local refractive-index. Since the knife edge alters the luminance depending on the refraction angle, schlieren photography presents an image where the pixel intensity is related to the refraction angle.[27] A calibration lens provides a quantifiable relationship between the refraction angle and the image pixel intensity.[28] The refraction angle ε provided by the calibration lens can be expressed as

$$\varepsilon \approx \tan \varepsilon = r/f, \tag{3}$$

where f and r are the focal length of the calibration lens and an arbitrary radius on the lens surface, respectively. A previous paper suggests using a calibration lens with a long focal length.[28] Having a longer focal length allows the uncertainty due to aberration to be neglected. This is because the focal plane of the calibration lens is far away from the camera sensor. In the present experiment, a plano-convex lens (CVI Laser
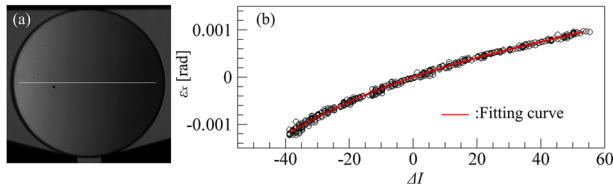
FIG. 3. Calibration using the vertical graded-filter cutoff. (a) Image pixel intensity change due to the calibration lens and (b) calibration curve obtained from the location indicating a white line shown on the calibration lens.

Optics, model: PLCX-25.4-5151.0-C, focal length: 10 m, outer radius: 12.7 mm, surface accuracy: $\lambda/10$) was employed as the calibration lens. Figure 3(a) shows the image pixel intensity provided by the calibration lens. The refraction angle ε_{image} appearing on the lens surface is expressed as follows:

$$\varepsilon_{image} = \varepsilon - \varepsilon_0 = \frac{1}{f}(r - r_0). \tag{4}$$

The subscript 0 denotes the defined centre of the calibration lens. Figure 3(b) shows the measured value and a fitting curve by a cubic polynomial. The calibration curve (fitting curve) shown in Fig. 3(b) enables the conversion of image pixel intensity to refraction angle. In the present setup, the available calibration value of the refraction angle is in the range between $0.974\,16 \times 10^{-3}$ and -1.2312×10^{-3} rad for the refractive index in the x-direction. Once the calibration value is obtained, the calibration lens is removed from the test section.

In the calibration process, the uncertainty of the refraction angle is mainly due to two factors: the approximation error of the fitting curve and the detection error of a virtual centre of the calibration lens. The virtual centre of the calibration lens is the location where the pixel intensity appearing on the surface of the calibration lens matches the background pixel intensity around the lens. The background pixel intensity is not perfectly uniform due to the scattering of the light source; thus, there is the possibility that the location of the virtual centre of the calibration lens moves. In Eq. (4), the virtual centre of the calibration lens related to r_0 has an error assumed as σ_{r0}, which results in the error of the refraction angle. On the other hand, the fitting curve produces the uncertainty of the refraction angle. Although the fitting curve shown in Fig. 3(b) shows good agreement with the experimental value, the approximation error cannot be neglected. The approximation error of the fitting curve is calculated by RMSE (Root Mean Squared Error) as

$$\sigma_{cal,y} = \sqrt{\frac{1}{N}\sum_{i=1}^{N}\left(\varepsilon_{exp,y}(\Delta I)_i - \varepsilon_{fit,y}(\Delta I)_i\right)^2}, \tag{5}$$

$$\sigma_{cal,x} = \sqrt{\frac{1}{N}\sum_{i=1}^{N}\left(\varepsilon_{exp,x}(\Delta I)_i - \varepsilon_{fit,x}(\Delta I)_i\right)^2}, \tag{6}$$

where N is the sampling number of the total obtained experimental values and ε_{exp} and ε_{fit} are the experimental and fitted calibration values, respectively. The subscripts x and y denote the cut-off direction. Therefore, the uncertainty of the refraction angle due to the calibration process is estimated using the following equations:

$$\sigma_{\varepsilon,y} = \sqrt{\left(\sigma_{cal,y}\right)^2 + \left[\left(\frac{\partial \varepsilon_{image,y}}{\partial r_{0,y}}\right)\cdot \sigma_{r0}\right]^2}, \tag{7}$$

$$\sigma_{\varepsilon,x} = \sqrt{\left(\sigma_{cal,x}\right)^2 + \left[\left(\frac{\partial \varepsilon_{image,x}}{\partial r_{0,x}}\right)\cdot \sigma_{r0}\right]^2}. \tag{8}$$

Figure 4 shows the flow chart for the processing of the schlieren images. The schlieren images are captured using the vertical- and horizontal-cutoff orientations separately. To reveal the anticipated weak density change created by the actuator, an image distorted by the density change due to plasma actuation is subtracted from a reference image which is captured before the experiment; namely, the subtracted image pixel intensity is expressed as $\Delta I(x, y) = I(x, y) - I_r(x, y)$, where I and I_r denote the distorted image intensity and the reference case, respectively. Based on the calibration curve, the subtracted image intensity $\Delta I(x, y)$ is converted to the refraction angle $\varepsilon(x, y)$. Each experiment was repeated three times to obtain an ensemble average of the local refraction angle $\hat{\varepsilon}(x, y)$. This process ensures the experimental repeatability. The derivative of the refractive index gradients forms an elliptic partial differential equation commonly known as the Poisson equation,

$$\frac{\partial^2 n(x, y)}{\partial x^2} + \frac{\partial^2 n(x, y)}{\partial y^2} = S(x, y) = \frac{n_\infty}{z}\left\{\frac{\partial \hat{\varepsilon}_x(x, y)}{\partial x} + \frac{\partial \hat{\varepsilon}_y(x, y)}{\partial y}\right\}, \tag{9}$$

where $S(x, y)$, which is the source term, is given by the refraction angle gradients obtained from the schlieren images. The Poisson equation is solved using the successive over-relaxation method. The local refractive-index, which is computed based on the solution of the Poisson equation (9), is related to the gas density by the Gladstone-Dale law,

$$n = k \cdot \rho + 1. \tag{10}$$

The Gladstone-Dale constant for air, $k = 2.26 \times 10^{-4}$ m³/kg, is applied in the calculation. Consequently, the spatial density distribution above the ns-DBD plasma actuator can be obtained.
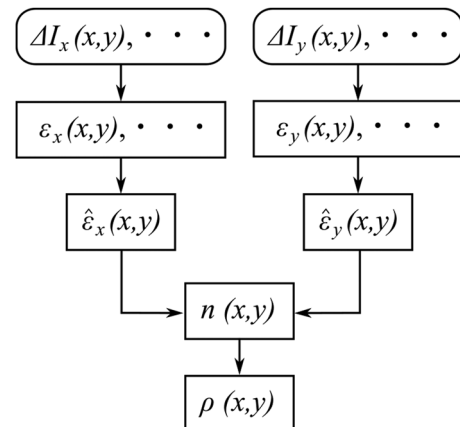

FIG. 4. The flow chart of the procedure for the quantitative density measurement.

D. Validation of the calibrated schlieren technique

Using the calibrated schlieren technique, the temperature distribution due to natural convection formed on an aluminum vertical hot plate of 150 mm × 1.6 mm (width × thickness) was measured and compared to a theoretical value to validate the present optical arrangement of calibrated schlieren photography. Based on a similarity solution of Eq. (11), the temperature T_{BL} in the thermal boundary layer formed on the vertical hot plate is calculated,

$$T_{BL} = H(\eta) \cdot (T_s - T_\infty) + T_\infty. \tag{11}$$

The function H is obtained from Ref. 29; a Prandtl number $Pr = 0.72$ is used for the present experiment. The similarity parameter η is expressed by Grashof number Gr at the distance y from the leading edge of the vertical hot plate,

$$\eta = \left(\frac{Gr}{4}\right)^{1/4} \cdot \frac{y}{x}, \tag{12}$$

$$Gr = \frac{g \cdot \beta \cdot (T_s - T_\infty) \cdot x^3}{\nu^2}, \tag{13}$$

where x, β, and ν are the perpendicular distance, thermal expansion, and kinematic viscosity, respectively. Gravity is taken as $g = 9.81$ m/s^2. The vertical plate was heated by a silicone rubber heater glued on the backside of the vertical plate, and the surface temperature was adjusted to $T_s = 326$ K using a DC power supply (Voltcraft, model: VSP 2410). The surface temperature was stable after the silicone rubber heater was switched on for more than 15 min. The surface temperature was measured using an IR camera (FLIR model: A655sc, accuracy: ±2 °C or ±2% of reading), confirming the uniform distribution on the entire surface. The room temperature and pressure are $T_\infty = 287.8$ K and $P_\infty = 102.47$ kPa, respectively.

Figure 5(a) shows the image pixel intensity distribution around the vertical hot plate. The parallel light beam passes through the width direction of the vertical plate. The schlieren image is captured using the graded-filter edge at the vertical-cutoff orientation. Therefore, the density is calculated using the one-dimensional Poisson equation because the density

gradient appears at only the x-direction. Thereafter, the density value is converted to a temperature using the ideal gas law. The temperature distributions calculated by the calibrated schlieren image and similarity solution are shown in Fig. 5(b). The experimental temperature distribution is in good agreement with the theoretical value. However, the temperature near the wall surface is slightly different because the light beam passing close to the wall surface is diffracted. The maximum uncertainty due to the calibrated schlieren technique is 0.80%. The maximum temperature difference between the averaged experimental curve and the theoretical curve is 0.70% and appears near the wall surface. Generally, the optical components and arrangement affect the accuracy in the calibrated schlieren technique. As the results of the present validation, the present optical components and arrangement lead to good accuracy which is similar to the previous work.[28]

III. RESULTS AND DISCUSSIONS

A. Qualitative flow characteristics

The shock waves as well as the thermal disturbance above the actuator are formed due to the rapid local gas heating. The qualitative density field shown in Fig. 6 was captured using the high-speed schlieren technique with the circular dot cut-off plate. The density gradient captured using the circular dot plate is sensitive to both directions on the x-y plane. As shown in Fig. 6(a), a hemi-cylindrical shock wave and a quasi-planar shock wave propagate from the edge of the exposed electrode and from the plasma streamers, respectively. The shock wave formation observed in the present experiment is identical to previous investigations.[17,24,30] Note that the shadow above the exposed electrode is the polyimide film that covers the lateral side edge of the exposed electrode and the connection cable (see Fig. 1); thus, we can neglect the physical effect of the shadow on the shock wave formation as well as the thermal disturbance. The plasma streamers propagate towards the ground electrode,[3] and the surrounding gas of the plasma streamers is rapidly heated because of the relatively higher temperature of the plasma layer. According to temperature measurements of the plasma layer,[16] the temperature increases by 40 K during the discharge phase at an input voltage of 18 kV in the first pulse. The thermal disturbance is not clearly observed at the elapsed time of approximately 0.14 μs in the schlieren image [Fig. 6(a)], whereas the shock waves have already formed. Although the surrounding gas is heated by the plasma discharge, the heated gas would be stationary at the elapsed time of approximately 0.14 μs. Since the thickness of the exposed electrode is 35 μm, the plasma layer would be thin; thus, density change of the plasma layer is barely visible immediately after the first plasma discharge event. At the elapsed time of 0.5 ms [Fig. 6(b)], the thermal layer can be observed as well as a hot plume. The hot plume is generated from the edge of the exposed electrode. Once a second plasma discharge event elapses [Fig. 6(c)], the second shock waves are formed; thereafter, the thermal layer and the hot plume grow slightly at the elapsed time of 1.5 ms [Fig. 6(d)].

The hot plume is advected towards the ground electrode due to a low-speed induced flow. After the elapsed time of
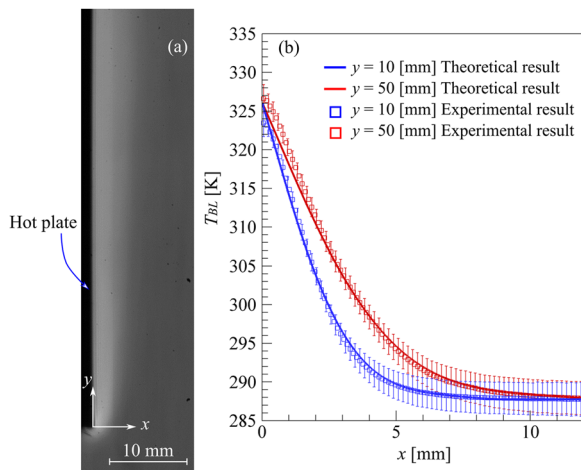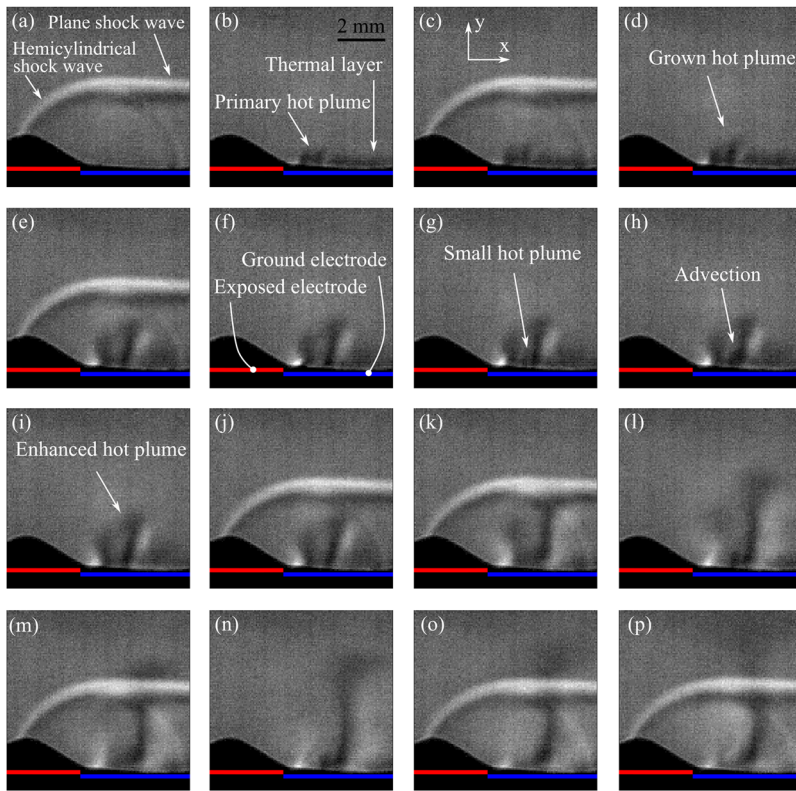

FIG. 5. The temperature distribution due to the natural thermal convection around the vertical hot plate. The theoretical result denotes temperature calculated by Eq. (11).

FIG. 6. The formation of the hot plume, thermal layer, and the shock waves. (a) $\Delta t = t_1 \approx 14$ μs, (b) $\Delta t = t_1 + 0.5$ ms, (c) $\Delta t = t_1 + 1.0$ ms, (d) $\Delta t = t_1 + 1.5$ ms, (e) $\Delta t = t_1 + 4.0$ ms, (f) $\Delta t = t_1 + 4.1$ ms, (g) $\Delta t = t_1 + 4.3$ ms, (h) $\Delta t = t_1 + 4.5$ ms, (i) $\Delta t = t_1 + 4.9$ ms, (j) $\Delta t = t_1 + 5.0$ ms, (k) $\Delta t = t_1 + 10.0$ ms, (l) $\Delta t = t_1 + 12.5$ ms, (m) $\Delta t = t_1 + 15.0$ ms, (n) $\Delta t = t_1 + 17.5$ ms, (o) $\Delta t = t_1 + 20.0$ ms, and (p) $\Delta t = t_1 + 30.0$ ms.

4 ms [from Fig. 6(e)], a small hot plume from the edge of the exposed electrode appears and moves towards the ground electrode. A smoke experiment by Roupassov *et al.*[3] showed that induced velocity is not zero; thus, the hot plume shown in the present experiment is advected due to the very low-speed ionic wind. The reason why the transfer of the hot plume cannot be observed in the present schlieren images at the range of the elapsed time of 0 and 4 ms is that the hot plume is relatively weak and propagates at a very slow velocity. Additionally, the plasma discharge would not generate a strong ionic wind at an early-stage of the actuator operation. Even though 5 ms elapsed from the first plasma discharge [Fig. 6(j)], the entire hot plume ascends due to the thermal convection; however, the hot plume gradually moves towards the ground electrode. This is because the low-speed ionic wind starts influencing the hot plume. The colour schlieren image, which shows the time-averaged density gradient of 2.5 ms, clearly captures the subsequent flow field of the advection event (Fig. 7). The orientation of the colour filter wheel used in the present experiment is also shown in Fig. 7. The undisturbed density field is indicated by the blue colour. The parallel light beam close to the edge of the exposed electrode bends towards the x-direction; namely, the hot plume moves towards the ground electrode due to forced convection. Additionally, it seems that the hot plume moves towards the upper right diagonal of the image. The ionic wind and/or an induced jet might cause the movement of the hot plume. On the other hand, the light beam above the ground electrode bends towards the y-direction; thus, natural convection caused by buoyancy force is dominant because the very weak ionic wind does not influence the heated gas (thermal layer) above the ground electrode. Since the hot plume leads to density change in both x-direction and y-direction, it is difficult to identify the hot plume in Fig. 7, whereas the green colour image appearing above the ground electrode is the thermal layer growing by buoyancy.

Although the shock wave interacts with the hot plume and thermal layer, the shock wave interaction should not strongly influence the thermal flow. As shown in Fig. 6, the shock wave propagates from the electrodes to surrounding air, interacting with the hot plume as well as the thermal layer. However, it seems that the thermal flow pattern hardly varies due to the shock wave interaction. According to an experiment[31] that the effect of the shock Mach number on gas bubble motion in a different density gas was investigated, in the case that a weak incident shock Mach number ($M \approx 1$) impinges on the bubble, the shape of a gas bubble with similar density to a surrounding gas hardly changes, whereas a large incident shock Mach number distorts the shape of the bubble. A shock wave
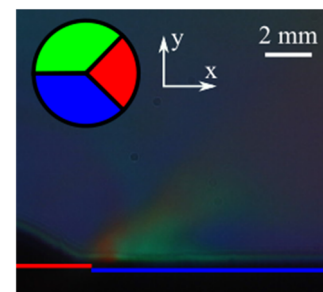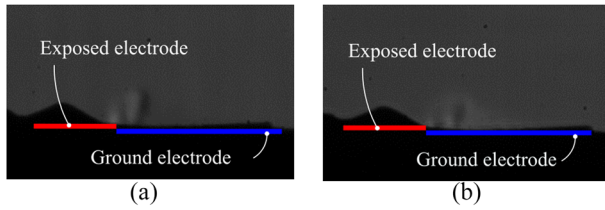

FIG. 7. Colour schlieren image.

FIG. 8. Typical schlieren images at Δt = 5 ms. (a) Pixel intensity change in the x-direction. (b) Pixel intensity change in the y-direction.

generated from the ns-DBD plasma actuator operated by few kilovolts propagates at approximately Mach 1.[20] Therefore, the hot plume and thermal layer do not strongly alter due to the shock wave interaction.

B. Quantitative flow characteristics

The calibrated schlieren technique converts the raw schlieren image to a quantitative density field. Figure 8 shows the typical schieren images at the elapsed time of 5 ms. Around the edge of the exposed electrode, a strong density change in the x-direction is present [Fig. 8(a)]; namely, it denotes the hot plume. The hot plume consists of the density change in the y-direction as well [Fig. 8(b)]. However, the thermal layer generated above the ground electrode is hardly observed in the density change of the x-direction. This is because the thermal layer, which would be not strongly affected by the ionic wind and the induced jet, ascends in the y-direction due to natural convection. Figure 9 shows the refraction angle distribution that is converted from the schlieren images of Fig. 8 through calibration. It is assumed that the induced flow by the ns-DBD plasma actuator is a two-dimensional phenomenon. An actual thermal flow generated by the plasma actuator is not a perfectly two-dimensional phenomenon; however, the thermal flow in the vicinity of the plasma actuator would be two-dimensional after time has elapsed. Note that the x = 0 mm indicates the edge of the exposed electrode. Moreover, the refraction angle distribution in the region where $y \leqq 1$ mm is unreliable as the light beam passing close to the wall surface is diffracted;

therefore, the uncertainty here would be large for the quantitative process. The refraction angle distribution, which is shown above y = 1 mm, is qualitatively the same as that of the image pixel intensity distribution of the schlieren images, but the refraction angle is quantifiable. The spatial density distribution, which is normalised by atmospheric density ρ_∞, is shown in Fig. 10. The hot plume appears between x = 1 and 2 mm above the ground electrode. Additionally, the thermal layer is extended to approximately x = 6 mm at the elapsed time of 5 ms.

The hot plume is enhanced due to several plasma discharges. Temporal variation of the spatial density distribution is shown in Fig. 11. The hot plume grows slightly at the elapsed time of 10 ms [Fig. 11(a)]; thereafter, the density caused by the hot plume decreases locally at the coordinate (x, y) = (2, 1) [from Figs. 11(b)–11(f)]. The movement of the whole hot plume towards the upper right diagonal is apparent from the spatial density distribution. The same behavior is observed in the qualitative images captured using the high-speed schlieren technique (Fig. 6). Figure 12 shows the density distribution along y = 1 mm. At the elapsed time of 1.0 ms when the second plasma discharge occurs, an almost uniform density distribution appears, although a weak density change can be observed at x = 1 mm. It is worth noting that the first plasma discharge occurs at the elapsed time of approximately 0 ms. At the elapsed time of 2.0 ms, the weak density change grows; namely, it denotes the hot plume. Since thermal convection by the plasma discharge does not immediately enhance the hot plume, both first and second plasma discharges cause the strong density change at the elapsed time of 2.0 ms. Although several plasma discharges cause the local density change, it seems that the enhancement of the density gradually decays from the elapsed time of 30 ms. This conclusion is reached because the minimum density of the hot plume changes 3.3% between the elapsed time of 0 and 10 ms, whereas it changes only 0.4% between the elapsed time of 30 and 50 ms.

The density of the hot plume is equilibrated with the surrounding gas density within several tens of milliseconds. The primary plasma discharges increase the gas temperature of the surrounding plasma layer; consequently, the density rapidly decreases within 3 ms (see Fig. 13). It is believed that the plasma-induced flow (the ionic wind and the induced jet) does not strongly affect the surrounding gas at this stage. At x = 0 mm, corresponding to the edge of the exposed electrode (Fig. 13), the density increases slightly after the rapid decrease. The ionic wind and/or the induced jet would begin to have an impact here, which results in this event. Thereafter, the density becomes almost uniform after the elapsed time
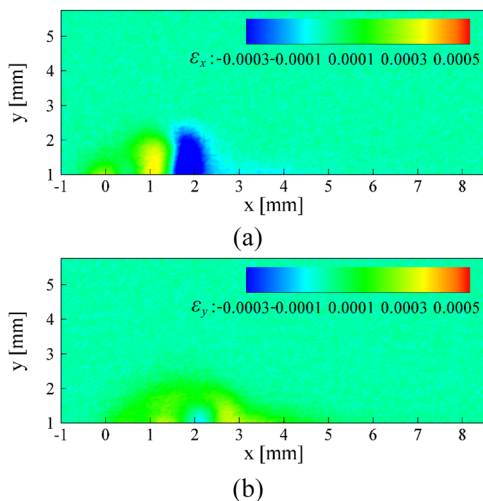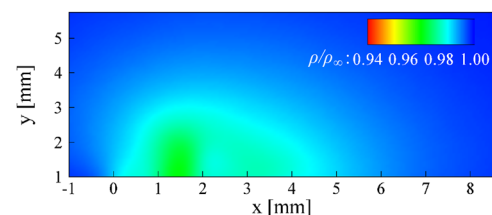

FIG. 9. Ensemble average of refraction angle distribution at Δt = 5 ms. (a) Refraction angle in the x-direction. (b) Refraction angle in the y-direction.

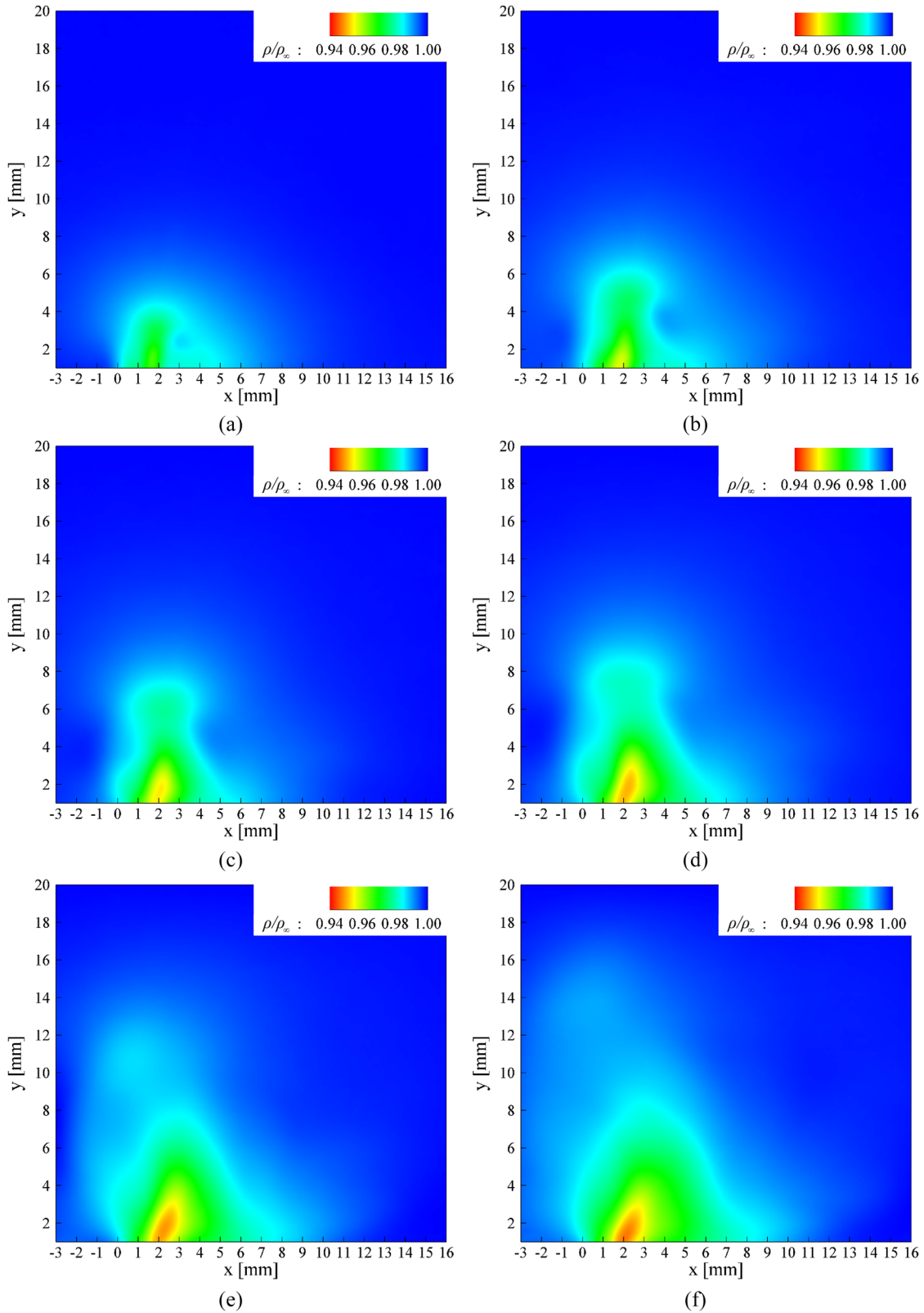FIG. 10. Spatial density distribution at Δt = 5 ms.

FIG. 11. Temporal variation of spatial density distribution. 101 times shock wave pulses occur during $\Delta t = 100$ ms. (a) $\Delta t = 10$ ms, (b) $\Delta t = 20$ ms, (c) $\Delta t = 30$ ms, (d) $\Delta t = 40$ ms, (e) $\Delta t = 70$ ms, and (f) $\Delta t = 100$ ms.

of 20 ms. The density history at $x = 1$ mm is similar to that of $x = 0$ mm; namely, the density change from 5 to 20 ms is caused by the ionic wind and/or the induced jet. However, the density at $x = 1$ mm is lower than the density at $x = 0$ mm. This is a result of the hot plume growth towards the ground

electrode. The movement of the hot plume leads to a further density decrease at the $x = 2$ mm location, which results in a density ratio of approximately 0.95 at the elapsed time of approximately 40 ms. Then, the density becomes uniform. At the $x = 3$ and 4 mm locations, the density did not decrease
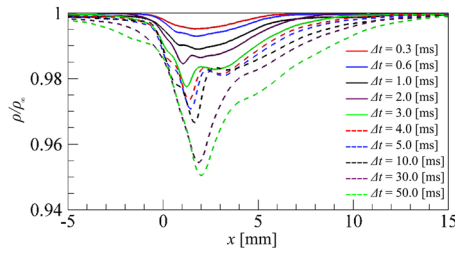
FIG. 12. Density distribution at $y = 1$ mm.
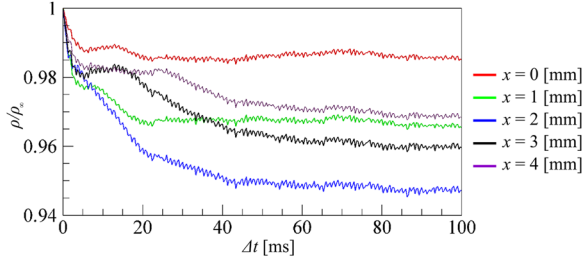
FIG. 13. Temporal variation of density decrease at $y = 1$ mm.

significantly compared with the $x = 2$ mm case; nevertheless, the plasma-induced flow is still apparent. This is because the core of the hot plume does not extend to more than $x = 3$ mm [Fig. 11(f)]. As shown in Fig. 13, the density is almost uniform after the elapsed time of 40 ms although the density at $x = 3$ and 4 mm keeps decreasing slightly. The reason why the density gradually decreases is due to natural convection of the thermal layer formed above the ground electrode.

The heated gas which moves away from the wall surface is not influenced by the plasma-induced flow (the ionic wind and the induced jet). Figure 14 shows the density profile along the y-coordinate. In the spatial density distribution above $y = 1$ mm, the first plasma discharge barely contributes to the hot plume enhancement. Consequently, both density profiles of the $x = 2$ and 3 mm positions at the elapsed time of 1 ms are similar to the temperature profile due to natural convection on a horizontal heated plate.[32] At the elapsed time of 5 ms, it can be observed that the thermal layer is slightly distorted
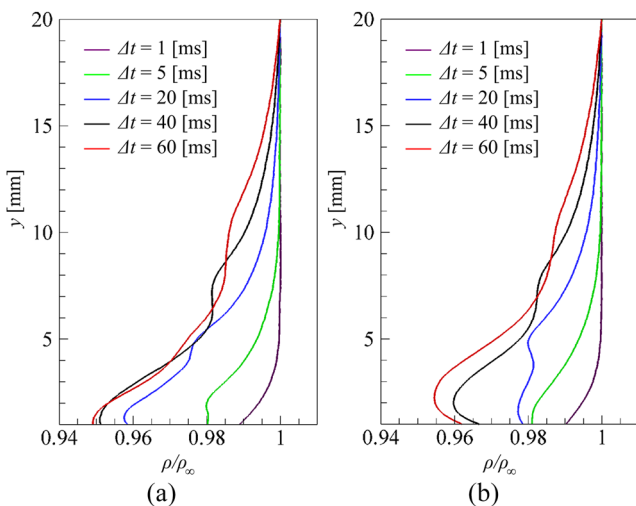
FIG. 14. Thermal layer distribution. (a) $x = 2$ mm and (b) $x = 3$ mm.

around $y = 2$ mm along $x = 2$ mm [Fig. 14(a)]. This is because the hot plume starts disturbing the thermal layer formed by the plasma layer. Note here that close to the wall surface (below $y = 1$ mm), the hot plume would start disturbing the thermal layer relatively early. In the density profile along $x = 3$ mm [Fig. 14(b)], the heated gas, which is generated by the primary discharges, begins to ascend after the elapsed time of 5 ms. The round-shaped profile appearing at the $y = 5$ mm location at the elapsed time of 20 ms moves to $y = 8$ mm, 20 ms later [Fig. 14(b)]. Even when the time elapses, the density intensity of the round-shaped profile visible at $y = 5$ mm is almost the same as that at $y = 8$ mm and that of $y = 10$ mm at the elapsed time of 60 ms. The same behavior occurs in the density profile along $x = 2$ mm [Fig. 14(a)]. However, this rounded shape will disappear due to thermal equilibrium in a steady state. Additionally, the density of the heated gas is equilibrated with the surrounding gas density when the heated gas moves further away from the wall surface. As shown in Figs. 11(a)–11(d), the heated gas above $y = 5$ mm ascends only in the y-direction even though the hot plume moves towards both x-direction and y-direction. The reason why the density intensity of the heated gas caused by the primary plasma discharges does not change above $y = 5$ mm is that the plasma-induced flow hardly influences the heated gas above $y = 5$ mm.

On the other hand, the density below the $y = 5$ mm location is strongly influenced by the plasma-induced flow. At the elapsed time of 5 ms (see Fig. 14), the density ratio, which is $\rho/\rho_\infty = 0.981$, at the coordinate $(x, y) = (3, 1)$ is similar to the density ratio of $\rho/\rho_\infty = 0.980$ at $(x, y) = (2, 1)$; thereafter, the density decreases slightly at the elapsed time of 20 ms, which results in a density change of 0.26% [Fig. 14(b)]. On the other hand, in the case of the density at $(x, y) = (2, 1)$, the local density decreases significantly, by 2.2%, at the elapsed time of 20 ms [Fig. 14(a)]. This is because the plasma-induced flow, which is the ionic wind and the induced jet, at first starts influencing the density field close to the edge of the exposed electrode. At the elapsed time of 40 ms, the density at $(x, y) = (3, 1)$ strongly decreases due to the hot plume being moved by the plasma-induced flow [Fig. 14(b)]. Moreover, the peak of the density decrease along $x = 3$ mm is located around $y = 2$ mm because the hot plume moves upwards along the y-direction.

IV. CONCLUSION

Qualitative and quantitative schlieren techniques were employed to investigate the spatial density distribution above a nanosecond pulsed dielectric barrier discharge (ns-DBD) plasma actuator in quiescent air. Consequently, qualitative schlieren showed that rapid heating at the edge of the exposed electrode generates a hemi-cylindrical shock wave and a hot plume. The hot plume is advected towards the ground electrode due to a low-speed induced flow which is caused by an ionic wind and/or an induced jet. On the other hand, the thermal layer formed due to thermal convection of the plasma streams above the ground electrode was not influenced by the low-speed induced flow. The quantitative schlieren revealed the detailed density distribution. The density of the hot plume

was enhanced due to several plasma discharges; however, the density is equilibrated with the surrounding gas density within several tens of milliseconds. Moreover, the heated gas which moves away from the wall surface was not influenced by the plasma-induced flow (the ionic wind and the induced jet), whereas the plasma-induced flow strongly influenced the density below $y = 5$ mm. This study showed the initial temporal variation of the spatial density distribution above the ns-DBD plasma actuator in quiescent air. Understanding how the thermal characteristics in quiescent air conditions interact with a boundary layer is important for a better understanding for the mechanism of boundary layer transition.

Nanosecond pulsed DBD plasma actuators provide thermal perturbation caused by local high energy transfer, and the thermal perturbation mainly leads to turbulent boundary layer transition. The fundamental thermal flow behavior shown in this study is that the thermal spot (hot plume) is locally generated and moves slightly. The possible scenario of the turbulent transition is that the local hot plume leads to strong and complicated thermal perturbation. The further studies focusing on the investigation of the energy transfer from the hot plume to the surrounding gas are important for the optimization of the ns-plasma actuators.

ACKNOWLEDGMENTS

[1]Y. Xiao, S. J. Dai, L. M. He, T. Jin, Q. Zhang, and P. H. Hou, "Investigation of film cooling from cylindrical hole with plasma actuator on flat plate," Heat Mass Transfer **52**, 1571–1583 (2016).

[2]P. Audier, M. Fenot, N. Benard, and E. Moreau, "Film cooling effectiveness enhancement using surface dielectric barrier discharge plasma actuator," Int. J. Heat Fluid Flow **62**, 247–257 (2016).

[3]D. V. Roupassov, A. A. Nikipelov, M. M. Nudnova, and A. Yu. Starikovskii, "Flow separation control by plasma actuator with nanosecond pulsed-periodic discharge," AIAA J. **47**(1), 169–185 (2009).

[4]J. R. Roth, "Aerodynamic flow acceleration using paraelectric and peristaltic electrohydrodynamic effects of a one atmosphere uniform glow discharge plasma," Phys. Plasmas **10**, 2117–2126 (2003).

[5]M. Riherd and S. Roy, "Serpentine geometry plasma actuators for flow control," J. Appl. Phys. **114**, 083303 (2013).

[6]S. Roy, P. Zhao, A. DasGupta, and J. Soni, "Dielectric barrier discharge actuator for vehicle drag reduction at highway speeds," AIP Adv. **6**, 025322 (2016).

[7]R. Spivey, R. Hewitt, H. Othman, and T. Corke, "Flow separation control on trailing edge radii using single dielectric barrier discharge plasma actuators: An application to vehicle drag control," in *The Aerodynamics of Heavy Vehicles II: Trucks, Buses, and Trains* (Springer, 2009), pp. 135–149.

[8]N. Benard, J. Jolibois, and E. Moreau, "Lift and drag performances of an axisymmetric airfoil controlled by plasma actuator," J. Electrost. **67**, 133–139 (2009).

[9]K. S. Choi, T. Jukes, and R. Whalley, "Turbulent boundary-layer control with plasma actuators," Philos. Trans. R. Soc., A **369**, 1443–1458 (2011).

[10]R. Erfani, H. Zare-Behtash, C. Hale, and K. Kontis, "Development of DBD plasma actuators: The double encapsulated electrode," Acta Astronaut. **109**, 132–143 (2015).

[11]M. Forte, J. Jolibois, J. Pons, E. Moreau, G. Touchard, and M. Cazalens, "Optimization of a dielectric barrier discharge actuator by stationary and non-stationary measurements of the induced flow velocity: Application to airflow control," Exp. Fluids **43**, 917–928 (2007).

[12]C. A. Borghi, A. Cristofolini, G. Neretti, P. Seri, A. Rossetti, and A. Talamelli, "Duty cycle and directional jet effects of a plasma actuator on the flow control around a NACA0015 airfoil," Meccanica **52**, 3661–3674 (2017).

[13]N. Benard and E. Moreau, "Capabilities of the dielectric barrier discharge plasma actuator for multi-frequency excitations," J. Phys. D: Appl. Phys. **43**, 145201 (2010).

[14]F. O. Thomas, T. C. Corke, M. Iqbal, A. Kozlov, and D. Schatzman, "Optimization of dielectric barrier discharge plasma actuators for active aerodynamic flow control," AIAA J. **47**(9), 2169–2178 (2009).

[15]K. Kinefuchi, A. Y. Starikovskiy, and R. B. Miles, "Numerical investigation of nanosecond pulsed plasma actuators for control of shock-wave/boundary-layer separation," Phys. Fluids **30**, 106105 (2018).

[16]A. Y. Starikovskii, A. A. Nikipelov, M. M. Nudnova, and D. V. Roupassov, "SDBD plasma actuator with nanosecond pulse-periodic discharge," Plasma Sources Sci. Technol. **18**, 034015 (2009).

[17]R. Dawson and J. Little, "Characterization of nanosecond pulse driven dielectric barrier discharge plasma actuators for aerodynamic flow control," J. Appl. Phys. **113**, 103302 (2013).

[18]G. Correale, T. Michelis, D. Ragni, M. Kotsonis, and F. Scarano, "Nanosecond-pulsed plasma actuation in quiescent air and laminar boundary layer," J. Phys. D: Appl. Phys. **47**, 105201 (2014).

[19]J. G. Zheng, Z. J. Zhao, J. Li, Y. D. Cui, and B. C. Khoo, "Numerical simulation of nanosecond pulsed dielectric barrier discharge actuator in a quiescent flow," Phys. Fluids **26**, 036102 (2014).

[20]Z. Zhao, J.-M. Li, J. Zheng, Y. D. Cui, and B. C. Khoo, "Study of shock and induced flow dynamics by nanosecond dielectric-barrier-discharge plasma actuators," AIAA J. **53**(5), 1336–1348 (2015).

[21]A. Komuro, K. Takashima, K. Konno, N. Tanaka, T. Nonomura, T. Kaneko, A. Ando, and K. Asai, "Schlieren visualization of flow-field modification over an airfoil by near-surface gas-density perturbations generated by a nanosecond-pulse-driven plasma actuator," J. Phys. D: Appl. Phys. **50**, 215202 (2017).

[22]H. Du, Z. Shi, K. Cheng, G. Li, J. Lu, Z. Li, and L. Hu, "The study of flow separation control by a nanosecond pulse discharge actuator," Exp. Therm. Fluid Sci. **74**, 110–121 (2016).

[23]D. Ullmer, P. Peschke, A. Terzis, P. Ott, and B. Weigand, "Impact of ns-DBD plasma actuation on the boundary layer transition using convective heat transfer measurements," J. Phys. D: Appl. Phys. **48**, 365203 (2015).

[24]J. Little, K. Takashima, M. Nishihara, I. Adamovich, and M. Samimy, "Separation control with nanosecond-pulse-driven dielectric barrier discharge plasma actuators," AIAA J. **50**(2), 350–365 (2012).

[25]A. Russell, H. Zare-Behtash, and K. Kontis, "Characterisation of ns-DBD plasma actuators for supersonic flow control," in Proceedings of 30th of the International Council of the Aeronautical Sciences, 2016.

[26]R. A. Dawson and J. Little, "Effects of pulse polarity on nanosecond pulse driven dielectric barrier discharge plasma actuators," J. Appl. Phys. **115**, 043306 (2014).

[27]G. S. Settles, *Schlieren and Shadowgraph Techniques: Visualizing Phenomena in Transparent Media* (Springer, 2001).

[28]M. J. Hargather and G. S. Settles, "A comparison of three quantitative schlieren techniques," Opt. Lasers Eng. **50**, 8–17 (2012).

[29]S. Ostrach, "An analysis of laminar free-convection flow and heat transfer about a flat plate parallel to the direction of the generating body force," NACA Technical Report 2635, 1952.

[30]K. Takashima, Y. Zuzeek, W. R. Lempert, and I. V. Adamovich, "Characterization of a surface dielectric barrier discharge plasma sustained by repetitive nanosecond pulses," Plasma Sources Sci. Technol. **20**, 055009 (2011).

[31]G. Layes, G. Jourdan, and L. Houas, "Experimental study on a plane shock wave accelerating a gas bubble," Phys. Fluids **21**, 074102 (2009).

[32]L. Pera and B. Gebhart, "National convection boundary layer over horizontal and slightly inclined surfaces," Int. J. Heat Mass Transfer **16**, 1131–1146 (1973).